Influence of precursor morphology and cathode processing on performance and cycle life of sodium-zinc chloride (Na-ZnCl$_2$) battery cells ☆

Louis Sieuw [a], Tu Lan [a,#], Enea Svaluto-Ferro [a], Fabrizio Vagliani [b], Sumit Kumar [c], Wenjin Ding [c], Alberto Turconi [b], Diego Basso [b], Andrea Pozzi [b], Corsin Battaglia [a,d], Meike V. F. Heinz [a,*]

[a] *Empa, Swiss Federal Laboratories for Materials Science and Technology, Dübendorf 8600, Switzerland*
[b] *FZSoNick S.A., Stabio 6855, Switzerland*
[c] *Institute of Engineering Thermodynamics, German Aerospace Center (DLR), Stuttgart, Germany*
[d] *ETH Zurich, Department of Information Technology and Electrical Engineering, Zürich 8092, Switzerland*

ARTICLE INFO

ABSTRACT

Replacing nickel by cheap and abundant zinc may enable high-temperature sodium-nickel chloride (Na-NiCl$_2$) batteries to become an economically viable and environmentally sustainable option for large-scale energy storage for stationary applications. However, changing the active cathode metal significantly affects the cathode microstructure, the electrochemical reaction mechanisms, the stability of cell components, and the specific cell energy. In this study, we investigate the influence of cathode microstructure on energy efficiency and cycle life of sodium-zinc chloride (Na-ZnCl$_2$) cells operated at 300 °C. We correlate the dis-/charge cycling performance of Na-ZnCl$_2$ cells with the ternary ZnCl$_2$-NaCl-AlCl$_3$ phase diagram, and identify mass transport through the secondary NaAlCl$_4$ electrolyte as an important contribution to the cell resistance. These insights enable the design of tailored cathode microstructures, which we apply to cells with cathode granules and cathode pellets at an areal capacity of 50 mAh/cm^2. With cathode pellets, we demonstrate >200 cycles at C/5 (10 mA/cm^2), transferring a total capacity of 9 Ah/cm^2 at >83% energy efficiency. We identify coarsening of zinc particles in the cathode microstructure as a major cause of performance degradation in terms of a reduction in energy efficiency. Our results set a basis to further enhance Na-ZnCl$_2$ cells, e.g., by the use of suitable additives or structural elements to stabilize the cathode microstructure.

1. Introduction

Commercial sodium-nickel chloride (Na-NiCl$_2$) batteries are suitable candidates for stationary energy storage applications. They provide a long shelf and cycle life [1], safe operation [2,3], and low environmental impact, but need to become more cost efficient to be deployed at large scale [4–6]. Adoption of a planar cell design may enhance manufacturability for this battery type, but at the cost of adding complexity related to mechanical stability, hermetic cell sealing, and the management of molten phases in the cell [7,8]. A reduction in operating temperature from ~300 °C to ≤200 °C would reduce both processing and operating costs by the use of polymer seals [9–11], but this decreases the

energy efficiency during cycling due to increased mass transport resistances [8]. An alternative approach to reduce cost consists in replacing nickel as active cathode metal by cheap and abundant zinc. Such Na-ZnCl$_2$ batteries offer a promising route to reduce the environmental footprint of this technology. Their study further provides fundamental insights into relevant design consideration for sodium-metal chloride cells, as replacing nickel by zinc affects the cell performance in several aspects.

Firstly, the choice of active cathode metal determines the cathode microstructure [12], which governs electronic and ionic transport. This is of particular importance for high-temperature sodium-metal chloride cells with high mass loading and areal capacity (e.g. ~0.3 g/ cm^2 and

~50 mAh/cm^2 in planar cells [10,13-15], ~1 g/ cm^2 and ~150 mAh/cm^2 in tubular cells [16]). In state-of-the-art Na-NiCl$_2$ cells, cathode granules are prepared from fine-grained filamentary Ni powder (Ni255, particle size 2.2 - 2.6 μm), which facilitates electronic percolation and mass transport [15]. However, zinc powders are presently not commercially available in similar (filamentary) form, and previous experimental studies on Na-ZnCl$_2$ cells applied powders of unspecified purity, morphology, or particle size [17–20]. While the effects of microstructural properties on electron and mass transport have recently been simulated for synthetic geometric models of Na-ZnCl$_2$ cathodes, experimental studies on this topics are lacking so far [21]. The cathode microstructure further determines the active metal content (proportion of metallic zinc reacting with NaCl to reach 100% SOC), for which both electronic percolation and ion transport are safely maintained during long-term battery cycling. Commercial Na-NiCl$_2$ batteries with favorable Ni255 morphology apply an active metal content of ~30% [22,23], and similar [18,19] or higher [13,24] values are required also for alternative cathode metals.

Secondly, the choice of active cathode metal governs the electrochemical reaction mechanisms. At present, the relevant (electro-)chemical processes and degradation mechanisms occurring for different metal cathodes in sodium-metal chlorides cells are only poorly understood. The de-/chlorination of a variety of different transition metals (i. e. Fe, Ni, Cu, Co, Mo) was investigated in the early stages of sodium-metal chloride battery development [25–29]. At that time, nickel-based compositions were identified to provide the longest cycle life [23,30,31], which was ascribed to their solid-state reactions during cycling. More recently, a variety of different cathode metals and metal combinations have been successfully applied both in planar, laboratory-scale sodium-metal chloride cells operated at ≤200 °C [14, 32-34], as well as in planar [8,15] and tubular cells [16,35] operated at ~300 °C. In Na-ZnCl$_2$ cells, the electrochemical reactions even involve liquid salt phases at intermediate state-of-charge (SOC) [17,18]. Furthermore, a recent study revealed chlorination of both nickel and iron electrodes to take place via dissolved metal ions in the secondary molten NaAlCl$_4$ electrolyte [36].

Thirdly, the ceramic Na-β''-alumina electrolyte applied in sodium-metal chloride cells was reported to undergo Na$^+$/Zn^{2+} ion exchange in molten ZnCl$_2$, which reduced its mechanical stability and increased its resistivity [37,38]. However, no signs of Na-β''-alumina degradation were reported for previous Na-ZnCl$_2$ cells over up to 50 cycles [16,18, 19], not even when cycled at a high temperature of 400 °C for 50 h [20].

Last but not least, the choice of active cathode metal determines the specific energy. Due to a lower cell voltage, the specific energy of Na-ZnCl$_2$ cells is approximately 20% lower than that of Na-NiCl$_2$ cells (assuming average equilibrium cell voltages of 2.0 V for Na-ZnCl$_2$ cells [17,18], and of 2.5 V for Na-NiCl$_2$ cells with mixed Ni/Fe electrode [15]). Nevertheless, zinc-based cathodes can be economically viable [17], and also their technical feasibility has previously been demonstrated: Planar Na-ZnCl$_2$ cells performed ~50 cycles in a capacity range between 20% and 90% SOC at temperatures between 190 °C and 280 °C, transferring cumulative capacities of up to 1.7 Ah/cm [2,17,18]. Addition of a carbon matrix to the cathode enhanced the rate capability and enabled cycling of zinc-based cathodes at an areal capacity of up to ~90 mAh/cm^2 for ~50 cycles (20–80% SOC, cumulative capacity 2.8 Ah/cm^2) [19]. Furthermore, our group recently integrated Zn/NaCl cathodes into large tubular battery cells with 38 Ah capacity (areal capacity ~150 mAh/cm^2), which performed >20 stable cycles at (20–80% SOC, cumulative capacity 2.1 Ah/cm^2) [16].

In this study, we relate the cycling performance of planar Na-ZnCl$_2$ cells to their cathode microstructure. We compare filamentary nickel and spherical, industry-grade zinc powders to demonstrate the influence of powder morphology, particle size, and active metal content on electronic percolation and relative density of Na-NiCl$_2$ and Na-ZnCl$_2$ model cathodes. Based on these results, we prepare additive-free Zn/NaCl cathode granules and cathode pellets, which are suitable for vacuum-infiltration with the molten secondary NaAlCl$_4$ electrolyte. We present cycling of planar Na-ZnCl$_2$ cells with 50 mAh/cm^2 areal capacity at 300 °C, demonstrate >200 cycles (10–90% SOC, cumulative capacity 8.9 Ah/cm^2), and discuss the cell voltage profiles with respect to the corresponding ternary phase diagram of NaCl, ZnCl$_2$, and AlCl$_3$. Comparison of cells with Zn/NaCl granules and pellets of the same composition reveals how the cathode microstructure affects cell resistance, specific energy, energy efficiency, and cycle life of Na-ZnCl$_2$ cells.

2. Material and methods

2.1. Model cathodes

For relative density and resistivity measurements of model cathodes, Zn/NaCl and Ni/NaCl pellets were prepared from microfine NaCl (purity 99.1–99.4%, 88 wt% < 45 μm), spherical Zn powder (purity >96%, ZnO 3%, particle size 3.5–5.0 μm, BET surface area = 0.28 m^2/g, UltraPure zinc dust UP4), and filamentary nickel powder (purity> 99.7%, particle size 2.2–2.6 μm, BET surface area = 0.64 m^2/g, type Ni255). Based on the underlying chlorination reaction, Zn (or Ni) + 2 NaCl ⇆ ZnCl$_2$ (or NiCl$_2$)+ 2 Na, the active metal content increases the molar ratio of Zn(or Ni)/NaCl according to $\frac{n(\text{Zn or Ni})}{n(\text{NaCl})} = \frac{1}{2 \cdot \text{active content}}$. These precursor powders were hand-mixed in a mortar before uniaxial compaction in a cylindrical die at variable pressure (0.8–1.3 kbar). The resistance of model cathodes was then measured at room temperature by placing the pellets (diameter = 15.5 mm, height ~1.1–1.6 mm) between two polished copper electrodes connected to a Keithley 2000 multimeter. The lower threshold resistance value of the instrument was 0.1 mΩ and was reached for several pellet compositions. The corresponding resistivities were approximated to 1 mΩ.cm.

2.2. Cathode granules and cathode pellets

The same precursor powders were used to prepare cathode granules and cathode pellets with 30% active metal content for cell cycling experiments. A Zn/NaCl cathode with 30% active metal content comprises a molar ratio of n(Zn)/n(NaCl)=5/3, and a mass ratio of m(Zn)/m (NaCl)= 64.9/35.1. The corresponding specific capacity amounts to 160 mAh/g. Cathode granules were prepared in batch sizes of 2 kg. After homogenization (roll milling, 4 h), the precursor powders (30% active metal content, Zn/NaCl=64.9 wt%/35.1 wt%, theoretical capacity 160 mAh/g) were compacted (Komarek B50A, roll force 35 kN), granulated (Komarek G100SA), and sieved to exclude particles larger than 1.6 mm. To resemble the particle size distribution of state-of-the-art granules, and to provide a suitable packing density for NaAlCl$_4$ vacuum infiltration, the fraction of fine particles < 212 μm in the granules was adjusted at 2.6 wt%, providing a tap density of 1.85 g/cm^3 (47% relative density).

While the cathode granules contained only Zn and NaCl, a fraction of the secondary NaAlCl$_4$ electrolyte (Sigma Aldrich, anhydrous, powder, 99.99%) was added to the cathode pellets as a solid powder. This served to provide additional pore space to enable vacuum infiltration, as well as a homogeneous distribution of molten NaAlCl$_4$ in the cathode pellets during cell cycling at elevated temperatures. For cathode pellets, the precursor powders (30% active metal content + NaAlCl$_4$, Zn/NaCl/ NaAlCl$_4$ = 52.1/27.9/20.0 wt%) were hand mixed and compacted in a cylindrical die at an uniaxial pressure of 0.67 kbar under inert atmosphere. In the presence of NaAlCl$_4$, the pellets (m = 1.25 g, diameter = 19.5 mm, thickness = 1.5 mm) had a density of 2.79 g/cm^3 (84% relative density). With respect to Zn and NaCl only, this corresponds to a relative density of 56% (9% higher than for granules). Scanning electron microscopy (SEM) images of granules and pellets (pristine and cycled) were obtained using a Nova NanoSEM 230 FEI, and the samples were protected in an Ar/N$_2$ atmosphere during the whole process using a transfer chamber. The granules, as well as the starting Zn, NaCl and NaAlCl$_4$ powders, were further analyzed through X-ray powder

diffraction (XRD) using a PANanalytical X'Pert PRO MRD, while the cycled pellet cathode material was put in a gas-tight domed sample holder and analyzed using an Empyrean diffractometer and an X'Celerator detector (Malvern Panalytical).

2.3. Assembly of planar high-temperature battery cells

For cell cycling, both cathode granules and pellets were inserted into laboratory-scale high-temperature cells (active cell area = 3.14 cm^2). These cells comprised a planar Na-β''-alumina electrolyte (1 mm thickness, ion conductivity 0.2 S/cm at 300 °C) with carbon coating on the anode side, which was sandwiched between two insulating α-alumina collars using a high-temperature glass sealing at 1010 °C. Details on the design and assembly of such cells were described in more detail in previous studies [15,39]. Cathode granules and cathode pellets were inserted into planar high-temperature cells at the same cathode mass loading of 0.32 g/cm^2 (1 g granules or 1.25 g pellet, both comprising 0.65 g Zn and 0.35 g NaCl). Then, the secondary electrolyte NaAlCl$_4$ was infiltrated under reduced pressure (<10 mbar) at a temperature of 200 °C (dwell time ≈30 min), compensating the NaAlCl$_4$ content of cathode pellets (0.5 g NaAlCl$_4$ for granules, 0.25 g for pellets). This resulted in a mass ratio of NaAlCl$_4$ to cathode materials (Zn, NaCl) of 0.5 in both types of cells. The corresponding molar composition in a phase diagram of (NaCl)$_2$, ZnCl$_2$, and AlCl$_3$ is 37.7 mol% AlCl$_3$, 62.3% (NaCl)$_2$ at 0% SOC. Considering two moles of NaCl facilitates extraction of pseudo-binary sections with constant AlCl$_3$ content, which represent the charge/discharge reaction in Na-ZnCl$_2$ cells in the presence of a secondary NaAlCl$_4$ electrolyte.

For cathode granules, a Ni foam (99.5% purity, 1.6 mm thickness, 95% porosity) and additional 0.2 g of NaAlCl$_4$ were added to the cathode side. This enhanced the electrical contact between current collector and the uneven surface of cathode granules [15], which was not necessary for cells with cathode pellets. For both granule and pellet cells, a disk of Na (99.9% purity, ~0.3 g, thickness ≈1 mm) was added on the anode side to facilitate Na plating in the first cycle. Ni cylinders served as current collectors for both the anode and cathode; their diameter was fitted to the inner diameter of the α-alumina collars to reduce potential leaking (molten Na and NaAlCl$_4$) to the minimum. The resulting assembly was closed off at both ends with stainless steel plates and circular graphite seals, six screws going through both plates and compressing the complete assembly; alumina washers were used for electrical insulation between anode and cathode. Springs were inserted between the Ni current collectors and the steel end plates, which were directly connected by nickel wires to ensure the electrical contact.

2.4. Electrochemical characterization

The cells were heated to and equilibrated at an operation temperature of 300 °C (± 5 °C) over a time period of ~8 h using a resistive coil heater (SAF KM-HC-GS). Cycling was performed using a Biologic VSP3e potentiostat with a combined constant-current and constant-voltage (CC—CV) procedure, limited by lower and upper cut-off voltages of 1.7 and 2.35 V and a cut-off current density of 0.1 mA/cm^2. As discussed previously for planar Na-NiCl$_2$ cells [8], we used the energy efficiency η_{energy} of Na-ZnCl$_2$ cells to determine their average resistance, R_{avg}, during cycling. During cycling in a defined SOC range (100% coulombic efficiency), this equals to the ratio of polarized discharge and charge voltages of the cell.

$$\eta_{\text{energy}} = \frac{V_{\text{eq}} - I_{\text{discharge}} R_{\text{avg}}}{V_{\text{eq}} + I_{\text{charge}} R_{\text{avg}}};$$

$$R_{\text{avg}} = \frac{V_{\text{eq}} \left(1 - \eta_{\text{energy}}\right)}{I_{\text{charge}} \eta_{\text{energy}} + I_{\text{discharge}}}$$

where η_{energy} is the energy efficiency, $I_{\text{charge/discharge}}$ is the charge/discharge current density. Corresponding to the equilibrium voltages

observed in phase regions I)-IV) of the phase diagram (see Fig. 3), we assumed an average equilibrium voltage V_{eq} of 2.03 V (40% at 1.92 V, 20% at 2.03 V, 15% at 2.09 V, 25% at 2.15 V).

2.5. Phase diagrams

The phase diagram mode of FactSageFactSage™ 8.1 was used to simulate the ternary phase diagram of (NaCl)$_2$-ZnCl$_2$-AlCl$_3$. In the simulations, the databases 'FactPS' and 'FTsalt' were selected. Considering two moles of NaCl facilitates extraction of pseudo-binary sections with constant AlCl$_3$ content, which represent the charge/discharge reaction in Na-ZnCl$_2$ cells in the presence of a secondary NaAlCl$_4$ electrolyte:

$$\text{Zn} + 2\ \text{NaCl} \leftrightarrow \text{ZnCl}_2 + 2\ \text{Na}.$$
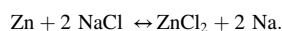
2.6. Electrical conductivity of Na-β''-alumina electrolyte

To determine the electrical conductivity of the Na-β''-alumina electrolyte after cycling, it was extracted from the cell and cut to a bar sample of ~1.0 × 3.5 cm^2, thickness ~1 mm. After removing the carbon coating and cleaning the surface, it was contacted in a custom-made 4-probe setup with spacing of l = 0.6 cm between the inner voltage probes, as described in more detail elsewhere[40,41]. The sample conductivity σ was determined during cool-down in a tube furnace, taking into account the sectional area of the bar sample A (~0.1 cm^2) and the probe spacing l, as σ = 1/R*l/A.

3. Results and discussion

In order to activate the theoretical capacity of an electrode during cell cycling, its microstructure needs to provide the transport of all relevant species to the reaction sites at the current densities (C-rates) of interest. This includes good contact between metal particles to provide electronic percolation. In theory, the higher molar weight and volume of Zn should facilitate electronic percolation in Zn/NaCl cathodes, compared to Ni/NaCl cathodes (M_{Zn}= 65.4 g/mol, $V_{\text{Zn,25°C}}$ = 9.2 cm^3/mol; M_{Ni}= 58.7 g/mol, $V_{\text{Ni,25°C}}$ = 6.6 cm^3/mol). Considering only metal and NaCl as the solid cathode constituents at 0% SOC, the same active metal content results in a higher metal weight and volume fraction in Zn/NaCl cathodes, compared to Ni/NaCl (Fig. 1a). For example, a Zn/NaCl cathode with an active metal content of 30% is composed of 36 vol% Zn and 64 vol% NaCl, while a corresponding Ni/NaCl cathode contains 28 vol% Ni and 72 vol% NaCl (at 0% SOC, not considering porosity or the secondary NaAlCl$_4$ electrolyte). In practice, however, it is the morphology of precursor powders which determines the relative density, and thereby the electronic percolation of high-temperature metal chloride cathodes.

For our study, we first prepared uniaxially pressed model pellets composed of Zn and NaCl, which can be processed outside a glovebox. We selected a fine-grained, industry-grade zinc powder with spherical morphology and a particle size of 3.5–5.0 μm, combined with a microfine NaCl. For comparison, we also prepared Ni/NaCl pellets with filamentary Ni255 powder (particle size 2.2–2.6 μm), as employed in state-of-the art Na-NiCl$_2$ battery cathodes. The particle size range and SEM images of these Ni255, Zn and microfine NaCl precursor powders are presented in Figure 2a-c. Model pellets with 30% active metal content and microfine NaCl feature significantly higher relative densities for spherical Zn powder, compared to filamentary Ni255 (by more than 10%, Fig. 1b). The influence of powder morphology on relative density of Zn/NaCl and Ni/NaCl model pellets persists at variable compaction pressures between 0.3 and 1.0 kbar: the relative density of model pellets increases from 72% to 83% with spherical Zn powder, and from 57% to 69% with filamentary Ni255 (Fig. 1b). Despite their higher relative density, Zn/NaCl model pellets display poorer electronic percolation than Ni/NaCl pellets, demonstrating the efficiency of filamentary metal powders to optimize the electronic backbone (Fig. 1c). In addition, the
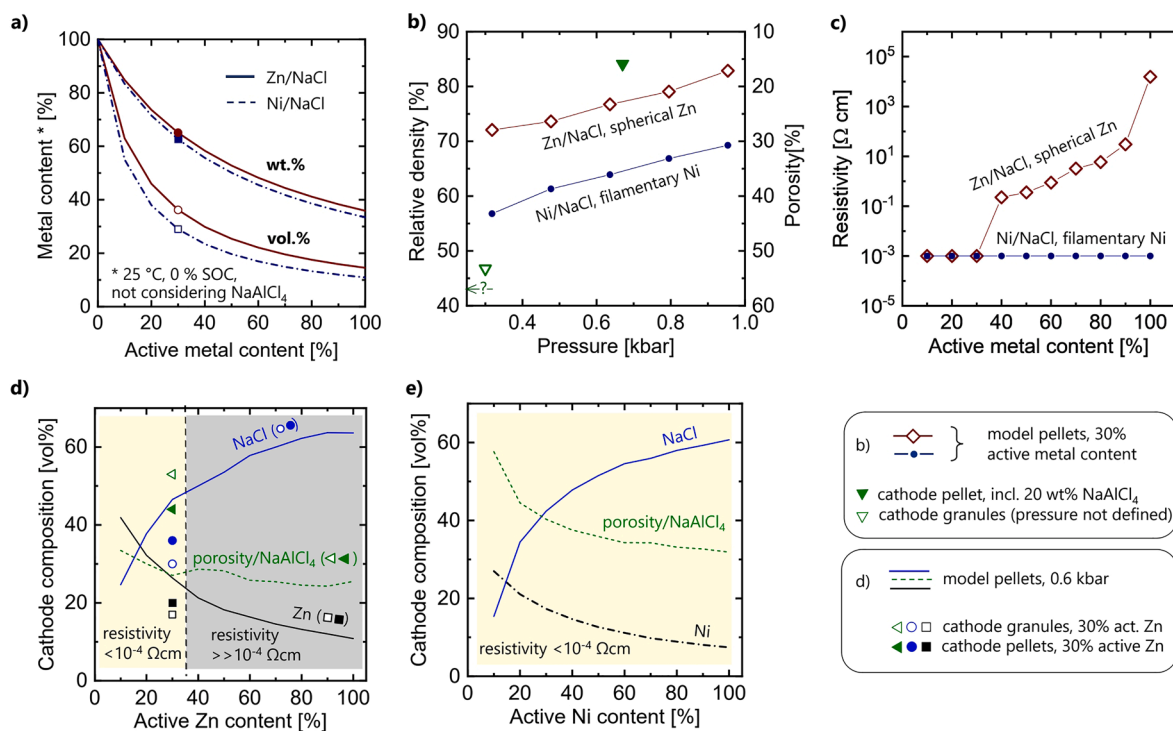
Fig. 1. Influence of metal choice and powder morphology on porosity and electrical percolation of Zn/NaCl and Ni/NaCl cathodes. a) Gravimetric (wt.%) and volumetric (vol.%) metal content of Zn/NaCl and Ni/NaCl cathodes with variable active metal content (not considering NaAlCl$_4$; volumes at 0% SOC, 25 °C). b) Relative density and porosity of model pellets with 30% active metal content compacted at variable pressures. Zn/NaCl pellets prepared from spherical metal powder have lower porosities than Ni/NaCl pellets prepared from filamentary Ni255 powder. c) Zn/NaCl model pellets maintain a low electrical resistivity at active metal contents ≤ 30%. d) The volumetric cathode composition of Zn/NaCl model pellets indicates stable electronic percolation at a metal content of 26 vol% and above with spherical Zn powder. e) With filamentary Ni255, electronic percolation is maintained even at 7 vol% Ni.

presence of ~3 wt% ZnO in the industry-grade zinc powder hinders electron transport in the Zn/NaCl pellet. While a low resistivity $<10^{-3}$ Ω cm is maintained for Ni/NaCl model pellets up to an active metal content of 100%, in Zn/NaCl model pellets this is only the case up to an active Zn content of 30%. Above this threshold, the resistivity increases by more than two orders of magnitude (to $>10^{-1}$ Ω cm). Combining the molar volumes and relative density, we display the volumetric compositions of Zn/NaCl and Ni/NaCl model pellets compacted at 0.6 kbar in Fig. 1d,e. The results of electrical resistivity measurements are also indicated. At an active metal content of 30%, at which electronic percolation is maintained, a Zn/NaCl model pellet comprises 26 vol% Zn, 47 vol% NaCl, and 27% porosity (Fig. 1d). At an active zinc content of 40% and above, where the resistivity increases significantly, the volume fraction of zinc decreases to 21 vol% and below. Models for random binary powder mixtures predict an electronic percolation threshold of ~20 vol% for a size ratio of 2 between the insulating phase (NaCl) and the metallic phase (Zn) [42]. The reported particles sizes and SEM images of microfine NaCl and spherical Zn indicate particle sizes of ~25 μm (Fig. 2c) and ~4 μm (Fig. 2b). This corresponds to size ratios above 5, at which electronic percolation would be expected even for metal contents below 10 vol%. This may indicate milling of NaCl and/or agglomeration of Zn particles during pellet preparation, which increase or decrease the effective particle size of NaCl and/or Zn in Zn/NaCl model pellets, thereby reducing their effective size ratio. With filamentary Ni255 powder, electronic percolation is maintained for all Ni/NaCl model pellets, despite low metal contents down to 7 vol% Ni (Fig. 1e). At an active metal content of 30%, Ni/NaCl model pellets comprise 17 vol% Ni, 43 vol% NaCl, and 40% porosity. This shows that a higher metal content is required for stable electronic percolation in Zn/NaCl cathodes prepared from spherical Zn powder, compared to

Ni/NaCl cathodes prepared from filamentary Ni255. In this study, we select Zn/NaCl cathodes with an active zinc content of 30% for the preparation of battery cells.

Apart from electronic percolation, percolation of the secondary molten NaAlCl$_4$ electrolyte is required in high-temperature sodium-metal chloride cathodes to provide ion transport to the surface of active materials (Zn and NaCl) during cell cycling. This is linked to the available pore space in the solid cathode, which is vacuum-infiltrated with molten NaAlCl$_4$. However, this process requires an open porosity with sufficiently large transport channels, which is not available in Zn/NaCl model pellets with <30% porosity. In the production of state-of-the-art Na-NiCl$_2$ batteries, the cathode materials are granulated to provide a bimodal pore size distribution, which is suitable for vacuum-infiltration [16,31]. We thus prepared Zn/NaCl and Ni/NaCl cathode granules in a similar manner. Furthermore, we adopted the preparation of pellets to increase the content of NaAlCl$_4$ in Zn/NaCl cathode pellets. To do so, we added a fraction of the secondary NaAlCl$_4$ electrolyte to the cathode materials in form of a coarse, solid powder (Fig. 2d). Zn, NaCl, and NaAlCl$_4$ powders were hand mixed and compacted under inert atmosphere, and the remaining fraction of NaAlCl$_4$ electrolyte was vacuum-infiltrated as for cathode granules (see supplemental information **SI section A, Figure S1**). For the present composition, compaction at 0.67 kbar resulted in reproducible vacuum-infiltration and stable cell cycling, as discussed further below.

SEM images of the microstructure of the surface of Zn/NaCl and Ni/NaCl granules are shown in Fig. 2e,f, and a Zn/NaCl cathode pellet with 20 wt% of NaAlCl$_4$ is shown in Fig. 2g. The morphology of Zn and NaCl particles is similar to the pristine state in both zinc granules and pellets (Fig. 2e,g), with larger rock salt particles (and NaAlCl$_4$ in the case of the pellet) loosely surrounded by zinc powder. This is in contrast to state-of-

a) spherical Zn, 3.5-5 µm   **b)** fil. Ni255, 2.2–2.6 µm   **c)** NaCl, <45µm   **d)** NaAlCl$_4$, 10-1000 µm

e) Zn/NaCl granule   **f)** Ni/NaCl granule   **g)** Zn/NaCl pellet (20 wt% NaAlCl$_4$)

h) schematic Zn/NaCl microstructure   **i)** schematic Ni/NaCl microstructure   **j)** schematic granule structure

k) schematic pellet structure

Zn/NaC granules / pellets
- **sperical Zn**, 17 / 20 vol.%
- NaCl, 30 / 36 vol.%
- porosity/NaAlCl$_4$, 53 / 44 vol.%

Ni/NaCl granules
- **filamentary Ni**, 14 vol%
- NaCl, 34 vol%
- porosity/NaAlCl$_4$, 52 vol%

- cathode material with intra-granular/ fine porosity
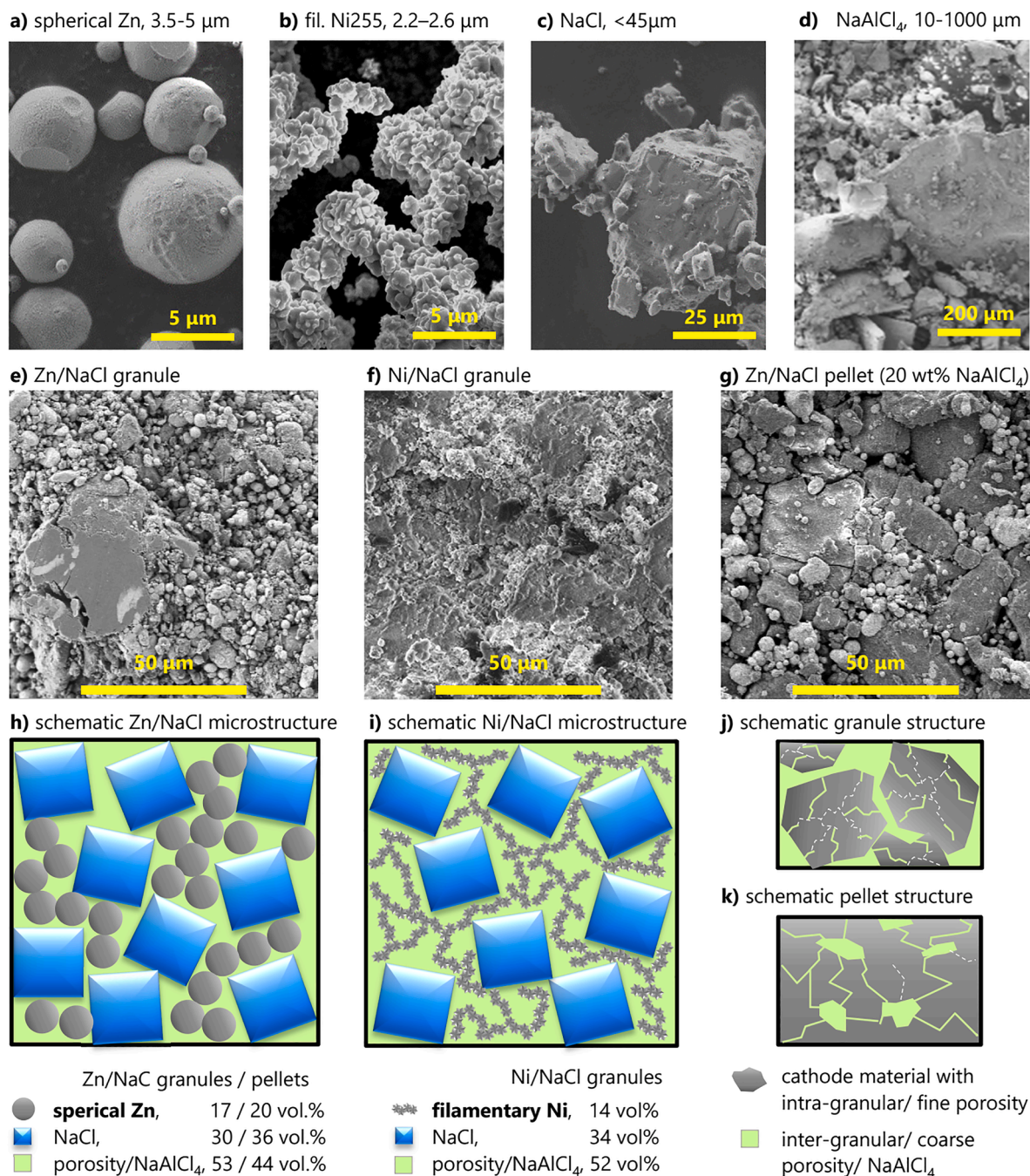- inter-granular/ coarse porosity/ NaAlCl$_4$

Fig. 2. Microstructure of metal and salt precursor powder and cathode composites. SEM images of a) spherical Zn, b) filamentary Ni255, c) microfine NaCl powder, d) NaAlCl$_4$ powder, e) Zn/NaCl granule, f) state-of-the-art Ni/NaCl granule, and g) Zn/NaCl pellet with 20 wt% NaAlCl$_4$. All cathode materials with 30% active metal content. Schematics showing the influence of powder morphology on h) Zn/NaCl and i) Ni/NaCl microstructure. Schematics showing the differences in intra-/inter-granular and fine/coarse porosity in j) cathode granules and k) cathode pellets. Pristine model cathodes (0% SOC) with spherical Zn have a higher packing density than those with filamentary Ni255. Still, the filamentary morphology of Ni255 facilitates electronic percolation.

the-art Ni/NaCl granules, where the NaCl particles appear compressed or smeared out (Fig. 2f). This indicates that the filamentary Ni255 particles not only affect metal percolation and porosity of Ni/NaCl granules, but also increase local compaction and shearing forces, which lead to deformation of NaCl particles. With a particle size distribution ranging from ~10 µm to ~1000 µm (Fig. 2d), the addition of NaAlCl$_4$ to the cathode pellets (Fig. 2g) decreases the electronic percolation threshold in the cathode pellets, compared to the microfine NaCl powder used in model pellets. The schematics in Fig. 2h,i summarize the

resulting microstructures for Zn/NaCl and Ni/NaCl cathodes. Based on a tap density of 1.85 g/cm^3, the Zn/NaCl granules have a relative density of 47%. This corresponds to 17 vol% Zn, 30 vol% NaCl, and 53 vol% porosity (these values are also indicated in Fig. 1b,d). The relative density of Zn/NaCl cathode pellets with NaAlCl$_4$ is as high as 84% (Fig. 1b). With a composition of 20 vol% Zn, 36 vol% NaCl, and 28 vol% NaAlCl$_4$, this translates to a combined pore and NaAlCl$_4$ content of 44 vol%. Despite a lower metal content, compared to the model pellets, both cathode granules and cathode pellets provided sufficient electronic

percolation (resistivity $<10^{-4}$ Ω cm, Fig. 1d). The schematics in Fig. 2j,k illustrate the different pore size distribution in cathode granules and cathode pellet. The pristine microstructure of cathode pellets provides a denser packing of active electrode materials, but less volume for ion transport through NaAlCl$_4$, compared to cathode granules. However, additional porosity and cracks were formed in both granules and pellets during subsequent vacuum-infiltration, and the same amount of NaAlCl$_4$ was successfully integrated into both cathode material forms.

In addition to these microstructural effects, a change from Ni/NaCl to Zn/NaCl cathodes affects the phase content in Na-ZnCl$_2$ cells during cycling at elevated temperatures. The binary phase diagram of NaCl and ZnCl$_2$ with an eutectic point at 253 °C has previously been related to the electrochemical processes observed during cycling of Na-ZnCl$_2$ cells [17, 18]. However, the presence of the secondary electrolyte NaAlCl$_4$ in Zn/NaCl cathodes further adds AlCl$_3$ to the system as a third component [43]. In Fig. 3a, we present the ternary phase diagram of (NaCl)$_2$, ZnCl$_2$, and AlCl$_3$ at 300 °C. Assuming thermodynamic equilibrium and the additional presence of excess Zn, the cathode composition in Na-ZnCl$_2$ cells progresses along a horizontal line in this phase diagram, as 2 mol of NaCl are consumed to chlorinate one mol of Zn, while forming Na at the anode with increasing SOC. The compositional variations of Zn/NaCl cathodes applied in this study (30% active metal content, mass ratio of NaAlCl$_4$ to cathode materials = 0.5) are indicated in Fig. 3a (37.8 mol% AlCl$_3$, 62.2–18.9 mol% (NaCl)$_2$, 0–43.3 mol% ZnCl$_2$), and the corresponding pseudo-binary phase diagram is displayed in Fig. 3b. The presence of AlCl$_3$ leads to the formation of Zn^{2+}-containing liquid phases with evolving composition (L$_1$, L$_2$), which decrease the temperature of the eutectic point to 240 °C. According to the phase regions in Fig. 3, the reversible chlorination and dechlorination of Zn at equilibrium conditions involves five successive reactions (shown below in unbalanced form). The NaCl-containing reactants providing the Cl$^-$ ions (left side) and the ZnCl$_2$-containg products (right side) are marked in bold.

   i) 0 – 17% SOC: Zn+ NaAlCl4 + **NaCl$_{(s)}$** ⇆ NaCl $_{(s)}$ + **L$_1$** (AlCl$_3$/ ZnCl$_2$/NaCl salt liquid) + Na

   ii) 17–50% SOC: Zn + **NaCl $_{(s)}$** + L1 ⇆ **Na$_2$ZnCl$_4$ $_{(s)}$** + L$_1$ (constant ZnCl$_2$ content) + Na

   iii) 50–58% SOC: Zn + L$_1$ + **Na$_2$ZnCl$_4$ $_{(s)}$** ⇆ **L$_1$** (ZnCl$_2$ content ↑) + Na

   iv) 58–69% SOC: Zn + **L$_1$** ⇆ **L$_1$** (ZnCl$_2$ content ↑) + Na

   v) 69–100% SOC: Zn + **L$_1$** ⇆ L$_1$ (ZnCl$_2$ content ↓) + **L$_2$** (ZnCl$_2$ content ↑) + Na

The number of components and phases present at the cathode of Na-ZnCl$_2$ cells affects their cell voltage profiles during electrochemical

cycling. According to Gibbs phase rule, only the formation of Na$_2$ZnCl$_4$ in phase region **ii**) is associated with a voltage plateau (see **SI section B**). Sloped voltage-capacity profiles are expected for all other phase regions (i, iii-v). This behavior in-line with results applying the galvanic intermittent titration technique (GITT) to a Na-ZnCl$_2$ cell at 300 °C. At a relaxation time of 60 min, the cell voltage stabilizes at 1.92 V up to 50% SOC. At higher SOC, the cell voltage increases continuously to 2.15 V (see **Figure S2**). However, different results are obtained when cycling Na-ZnCl$_2$ cells at relevant rates.

We present cycling results of cells with Zn/NaCl cathode granules and pellets at 300 °C at a mass loading of 0.32 g/cm^2 in Fig. 4. As for other Na-NiCl$_2$ batteries, the theoretical capacity of Na-ZnCl$_2$ cells is defined based on the complete electrochemical reaction of NaCl with the metal constituents of the cathode (Q$_T$ = 160 mAh/g, areal capacity 51 mAh/cm^2; 1C = 160 mA/g, 51 mA/cm^2). To avoid over(dis)charge reactions involving NaAlCl$_4$, we applied both capacity and voltage limitations during cycling (100% SOC at 160 mAh/g; 1.7 V - 2.35 V). In the first (maiden) cycle at 3 mA/cm^2, both cells assembled with Zn/NaCl cathode granules (Fig. 4a) and cathode pellet (Fig. 4b) reach their theoretical capacity (100% SOC) within the voltage limits. Thus, all NaCl was consumed to chlorinate the coarse Zn particles, even in the absence of additives, and despite the presence of ZnO. For the consecutive rate tests at 5, 10 and 15 mA/cm^2 (Fig. 4c,d), we restricted the capacity range to 10–90% SOC (128 mAh/g). Cycling proceeded within the voltage limits at 5 and 10 mA/cm^2, while at 15 mA/cm^2 the end of charge (80–90% SOC) occurred at constant voltage (cut-off voltage = 2.35 V). The voltage profiles of Na-ZnCl$_2$ cells with cathode granules and cathode pellets show several characteristic features, such as voltage fluctuations, a voltage hysteresis, and a defined succession of voltage plateaus and slopes. We first discuss these features, before analyzing the performance of Na-ZnCl$_2$ cells in terms of cell resistance, rate capability, and energy efficiency further below.

In some capacity regions (Fig. 4a-d), the cell voltage fluctuates by ± 50 mV, resulting in a noisy voltage profile. Voltage fluctuations are more pronounced in the first (maiden) cycle and during charge (e.g. at 40–50% SOC and 70–100% SOC for Zn/NaCl granules, Fig. 4a). Such a behavior was not observed in our previous studies on Na-NiCl$_2$ cells [8, 15], or in other reports on Na-ZnCl$_2$ cells [17-20]. In part, we ascribe the voltage noise to unstable percolation of the coarse Zn metal backbone (and/or its contact to the current collector). The microstructure of Zn/NaCl cathodes with spherical zinc particles stabilizes upon electrochemical plating during cycling, but is further disturbed by a volume decrease of active materials upon charge (e.g. consumption of NaCl) [16]. Voltage fluctuations persist in subsequent cycles mainly for cells
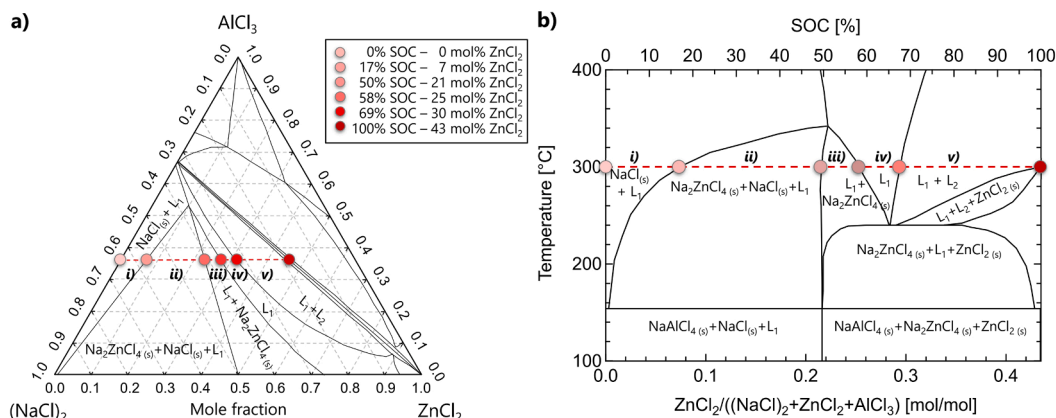

Fig. 3. Phase diagrams representing the phase content expected in the cathode of Na-ZnCl$_2$ cells at thermodynamic equilibrium. a) Ternary phase diagram of (NaCl)$_2$, ZnCl$_2$ and AlCl$_3$ at 300 °C, 1 atm., and b) corresponding pseudo-binary section. The compositional changes expected in the Zn/NaCl cathode at variable SOC cover 5 phase regions (i-v).
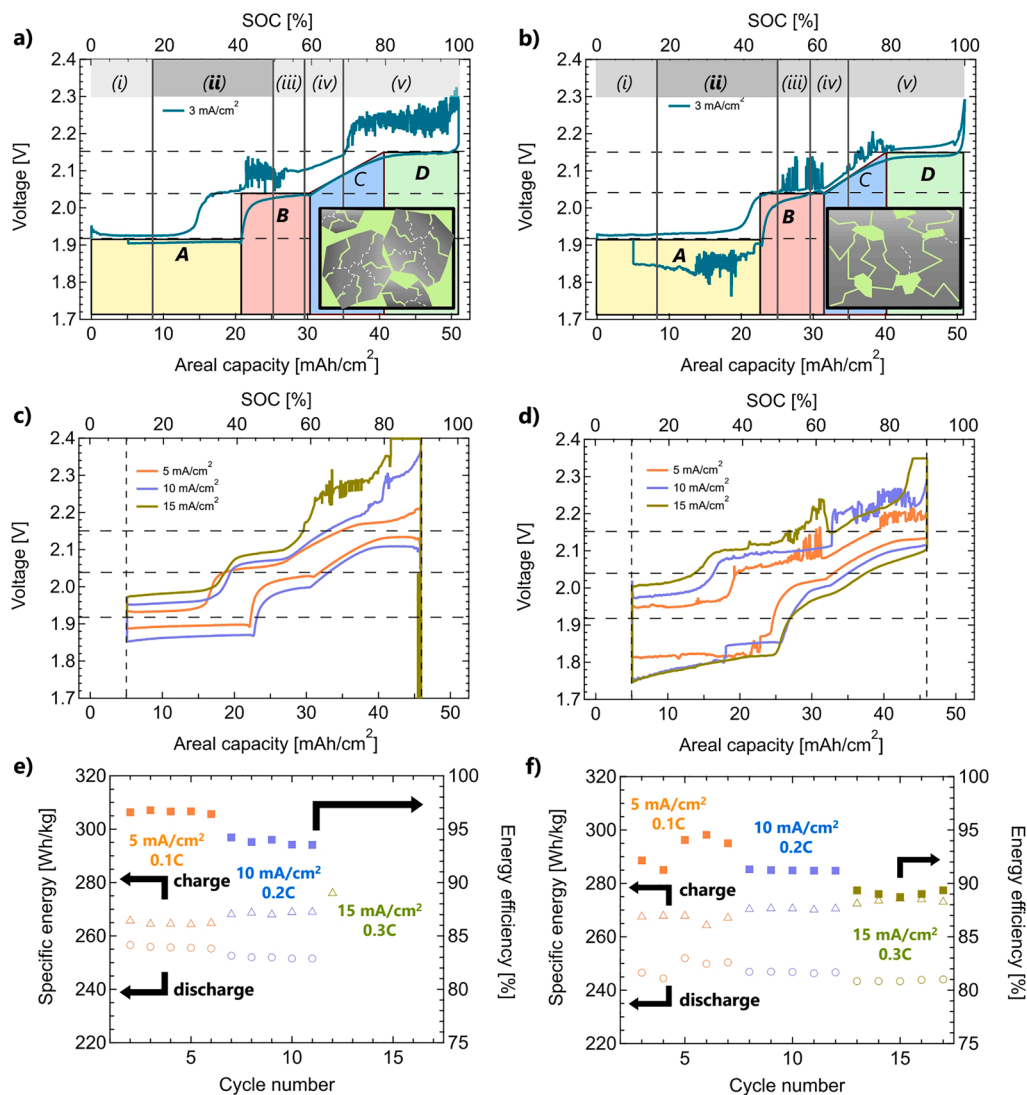
Fig. 4. Electrochemical cycling of Na-ZnCl₂ cells with cathode granules and cathode pellet (30% active Zn) at 300 °C. Voltage-capacity profiles of the first (maiden) cycles for **a)** cathode granules and **b)** cathode pellet. Insets: schematic representation of the microstructures of cathode granules and cathode pellet. Voltage-capacity profiles at subsequent cycles at variable current densities for **c)** cathode granules and **d)** cathode pellet. Dis-/charge energy and energy efficiency per cycle for **e)** cathode granules and **f)** cathode pellet.

with cathode pellet, indicating that mass transport through molten NaAlCl₄ may be limited, compared to cells with cathode granules. Additional voltage fluctuations occur at overall increased overpotentials towards the end of discharge in cells with cathode pellet (e.g. 45–20% SOC, Fig. 4b). In this case, the re-precipitation of NaCl may temporarily hinder the transport of ions through the secondary molten salt electrolyte at the cathode.

Overall, the voltage profiles of granule and pellet cells display a similar succession of plateaus and slopes, and thus a similar phase evolution. In contrast to the phase diagram, the measured voltage profiles indicate the presence of three voltage plateaus: **A** at approximately 0–40% SOC, B at 40–60% SOC, and **D** at 75–100% SOC (Fig. 4a-b). Only in one region, **C**, at 60–75% SOC, the voltage profiles are markedly sloped. This is in contrast to the ternary phase diagram with one voltage plateau (*ii, dark gray region in Fig. 4a-b*), suggesting that the phases formed during cell cycling are not in thermodynamic equilibrium. In particular, the oxidized Zn²⁺ species seem to form separate phases, instead of mixing with molten NaAlCl₄. This reduces the degree of freedom, in line with the observed voltage plateaus. In the simplest case, the resulting phase regions correspond to those of the binary NaCl-ZnCl₂

system [17,18]. Again, the NaCl-containing reactants providing the Cl⁻ ions (left side) and the ZnCl₂-containing products (right side) are marked in bold.

A) 0 - 40% SOC, 1.92 V Zn + **NaCl** $_{(s)}$ ⇆ **Na₂ZnCl₄** $_{(s)}$ + Na
B) 40 - 60% SOC, 2.04 V Zn + **Na₂ZnCl₄** $_{(s)}$ ⇆ L₁ (ZnCl₂/NaCl salt liquid) + Na
C) 60 - 75% SOC, 2.04 - 2.15 V Zn + L₁ ⇆ L₁ (ZnCl₂ content ↗) + Na
D) 75 - 100% SOC, 2.15 V Zn + L₁ ⇆ **ZnCl₂** $_{(s)}$ + Na

To summarize these observations, we present a graphical illustration of the reaction mechanisms expected for the ternary phase diagram in Fig. 5a. Possible reaction mechanisms representing the electrochemical cycling data and corresponding to the binary system are shown in Fig. 5b.

We determined the equilibrium potentials stated above by averaging the voltages at the start of charge and discharge plateaus in the maiden cycles (dashed lines in Fig. 4a-d). This was confirmed by corresponding differential capacity plots (dQ/dV, see **SI section C, Figure S3**). Thus, region **A**) in the voltage profiles at 1.92 V involves the consumption of

all accessible NaCl to form Na_2ZnCl_4. In region **B**), a liquid phase (L_1) is formed from Na_2ZnCl_4 at 2.04 V. Formation of a single salt liquid phase (L_1) in region **C** leads to a sloped voltage profile: its evolving composition (increasing and decreasing contents in $ZnCl_2$ and NaCl, respectively) leads the cell voltage to increase gradually. Finally, $ZnCl_2$ precipitates from this liquid salt in region **D**) at 2.15 V. The average equilibrium voltage V_{eq} for this type of Na-$ZnCl_2$ cell amounts to ~2.03 V.

Based on the voltage profiles, cells with cathode pellet generally show higher overpotentials and stronger voltage fluctuations than cells with cathode granules, in particular at SOC <60% SOC (Fig. 4c-d). This may be related to their lower porosity/ $NaAlCl_4$ content (44 vs. 53 vol%, Fig. 2g,h), which limits mass transport through the thick cathode. The voltage profiles of pellets further show a hysteresis at intermediate SOC (Fig. 4c,d, e.g. 30–50% SOC). The origin of this hysteresis lies in an earlier transition from phase region **A**) to **B**) during charge, compared to discharge. This suggests the presence of additional overpotentials occurring towards the end of phase region **A**) in the charge reaction between Zn and NaCl. For cells with cathode pellet, the voltage hysteresis broadens significantly with increasing current density, again indicating mass transport limitations in this region. Furthermore, the overpotentials are higher in cathode pellets throughout discharge in region **A**), where Na_2ZnCl_4 decomposes to Zn and NaCl. For cathode granules, the voltage hysteresis decreases as the microstructure of cathode granules stabilizes during the first cycles at low current density (compare Fig. 4c at 5 and 10 mA/cm², 30 – 45% SOC). As shown by a schematic representation in Fig. 4a, the cathode granules present a bimodal inter- and intra-granular porosity, with large pore channels between granules. The decreasing voltage hysteresis during the first cycles (Fig. 4c) indicates that the intra-granular porosity is initially not completely filled with $NaAlCl_4$. During the subsequent reaction steps, the cycled cathode materials rearrange, enabling access also to the active materials inside the granules. The lower porosity in cathode pellets results in higher mass transport resistances, compared to granules. However, the distribution of $NaAlCl_4$ is more homogeneous from the beginning, and all active materials are accessible during charge in

region **A**). To verify this hypothesis, we mortared cathode granules to a fine powder, which we then used to assemble a cell with 20 wt% $NaAlCl_4$ as done for regular cathode pellets (see **Figure S4**). This resulted in a similar voltage profile at intermediate SOC, confirming that mass transport limitations in the granule microstructure are indeed responsible for the hysteresis. Furthermore, the pellet cathode assembled from mortared granules does not show increased overpotentials during discharge at low SOC (region **A**). Both observations confirm the influence of cathode microstructure on the accessibility of active material during cycling. Thus, mass transport through the $NaAlCl_4$-filled pore channels limits cycling of the present Na-$ZnCl_2$ cells.

Mass transport limitations and overpotentials further affects the rate performance and energy efficiency, which is summarized in Fig. 4e,f for both types of cells. The specific charge and discharge energies are displayed for each cycle, along with the calculated roundtrip energy efficiency (equal to the voltage efficiency since the cell was cycled within a constant 10–90% SOC window). For the cell with cathode granules, the discharge energy decreases from 256 to 252 Wh/kg when increasing the discharge current from 5 to 10 mA/cm², with respective energy efficiencies of 97% and 94%. For the pellet cell, the discharge energy decreases from 252 to 243 Wh/kg when increasing the discharge rates from 5 to 15 mA/cm², with respective energy efficiencies of 94% and 89%. Together with the average equilibrium voltage of 2.03 V, these energy efficiencies can be used to estimate the average cell resistance, which amounts to ~6 Ω cm² for the cell with cathode granules cells. For the cell with cathode pellet, the average cell resistance decreases in the first 17 cycles, from ~12 Ω cm² at 5 mA/cm² to ~8 Ω cm² at 15 mA/cm². This trend is also confirmed by impedance measurements performed at 10% SOC upon discharge (see **Figure S5**). All other cell components as well as the cycling conditions being the same, differences in cell resistance of ≥2 Ω cm² are fully ascribed to microstructural effects in the cathode pellet. In particular, larger pore channels in cells with cathode granules result in lower mass transport limitations through molten $NaAlCl_4$, compared to cathode pellets. However, despite a lower cell resistance, the cycle life of cells with cathode granules was limited (see **Figure S6** for examples of other cells of the same type). Associated with
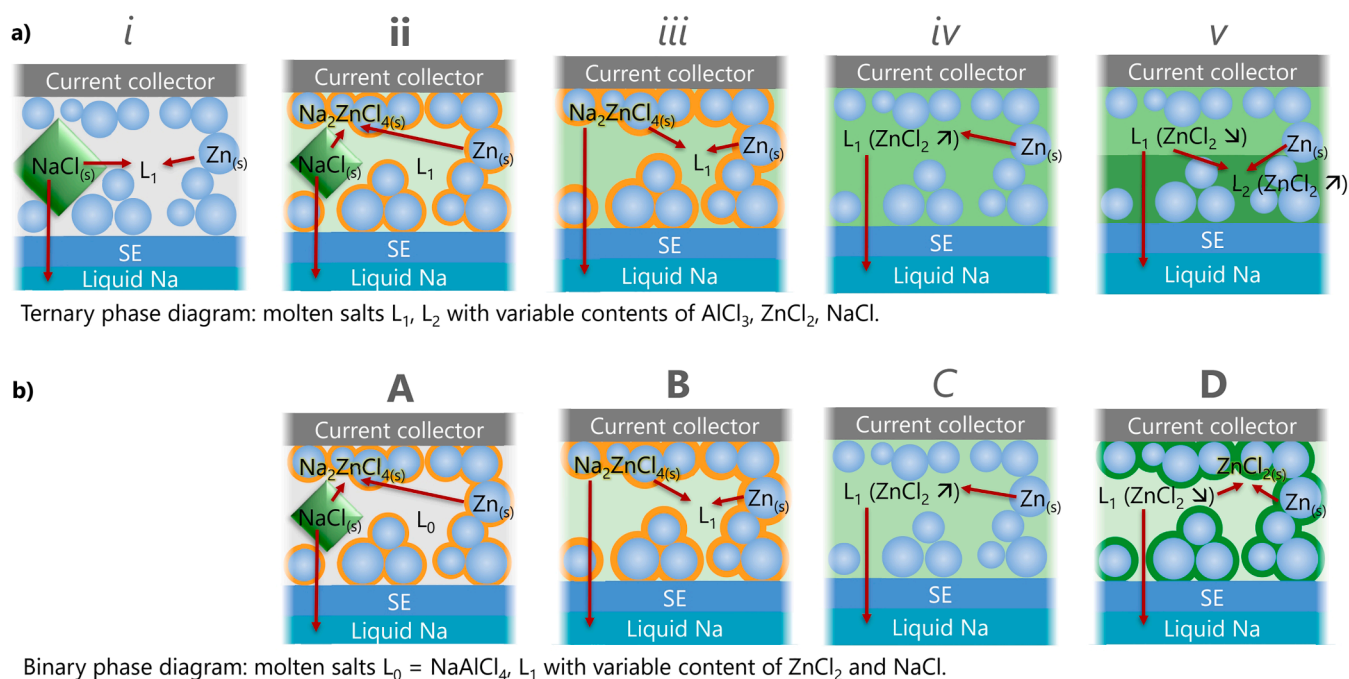

Fig. 5. Reaction mechanisms expected in Na-$ZnCl_2$ cells based on the ternary phase diagram ($NaCl_2$, $ZnCl_2$, $AlCl_3$), compared to those of the binary phase diagram ($NaCl_2$, $ZnCl_2$). **a)** In the ternary system, the Gibbs phase rule suggests a voltage plateau for reaction **ii**, but sloped voltage-capacity profiles for reactions i, iii, iv, and v. **b)** The cycling results indicate the presence of three voltage plateaus **A, B, D** and one sloped region C.

a progressive voltage increase towards the end-of-charge, cells with cathode granules were prone to an early cell failure. Based on visual inspection after disassembly, the bimodal microstructure rearranged during cycling in cells with cathode granules, thereby affecting electronic and/or ionic percolation. Capturing the relevant microstructural changes responsible for cell failure by scanning electron microscopy is challenging, and images obtained after vacuum infiltration with NaAlCl$_4$, cool-down to room temperature, and extraction of the cathode material from the cell are difficult to interpret (**Figure S7**). Nevertheless, our cycling results clearly indicate that the spherical morphology of Zn powder not only affects packing density and electronic percolation of Zn/NaCl cathodes, but also their mechanical integrity. The cell with cathode granules in Fig. 4a,c,e failed after one charge at 15 mA/cm^2, completing eleven full charge-discharge cycles (including the maiden cycle) with a cumulative capacity of 1.4 Ah.

For the cell with cathode pellet, cycling was continued at 10 mA/cm^2 (Fig. 6a-b). The cell performed 200 additional cycles (after the first 17 cycles, i.e. maiden cycle and rate test cycles, 2.2 Ah), resulting in a total cumulative capacity of 8.9 Ah/cm^2 (217 cycles at 10 – 90% SOC). During its life, the cell remained at a temperature of 300 °C for 82 days

(1968 h). With cycling, charge energies increased (from 270 to 280 Wh/kg, +4%) and discharge energies decreased (from 248 to 233 Wh/kg, −6%), resulting in decreasing energy efficiencies between 92% and 83% (Fig. 6b). We ascribe this to an increase in overpotentials, which is most significant during discharge of cycles 50 to 130. Applying a combined constant-current and constant-voltage procedure, a coulombic efficiency of 100% was maintained until cycle 127 (5.2 Ah/cm^2), after which the coulombic efficiency oscillated around 99.8% (Fig. 6c, see **Figure S8** for voltage-capacity profiles up to cycle 217). Thus, the cycling performance of the cell with cathode pellet can be expressed in terms of its average cell resistance (Fig. 6d). A decreasing cell resistance in the first 17 cycles indicates beneficial changes to the pellet microstructure, e.g. by enhanced percolation (necking) of the metal backbone, or by widening the initially narrow NaAlCl$_4$ transport channels. Over the subsequent 200 cycles performed at 10 mA/cm^2, the average cell resistance progressively increased from 8.5 to 18.5 Ω cm^2. A pronounced phase of degradation occurs between cycle 50 and 130, where the average cell resistance increases from 10 to 16 Ω cm^2. Conductivity measurements on the Na-β′′-alumina electrolyte extracted from the cell after cycling showed slightly lower values compared to a fresh reference
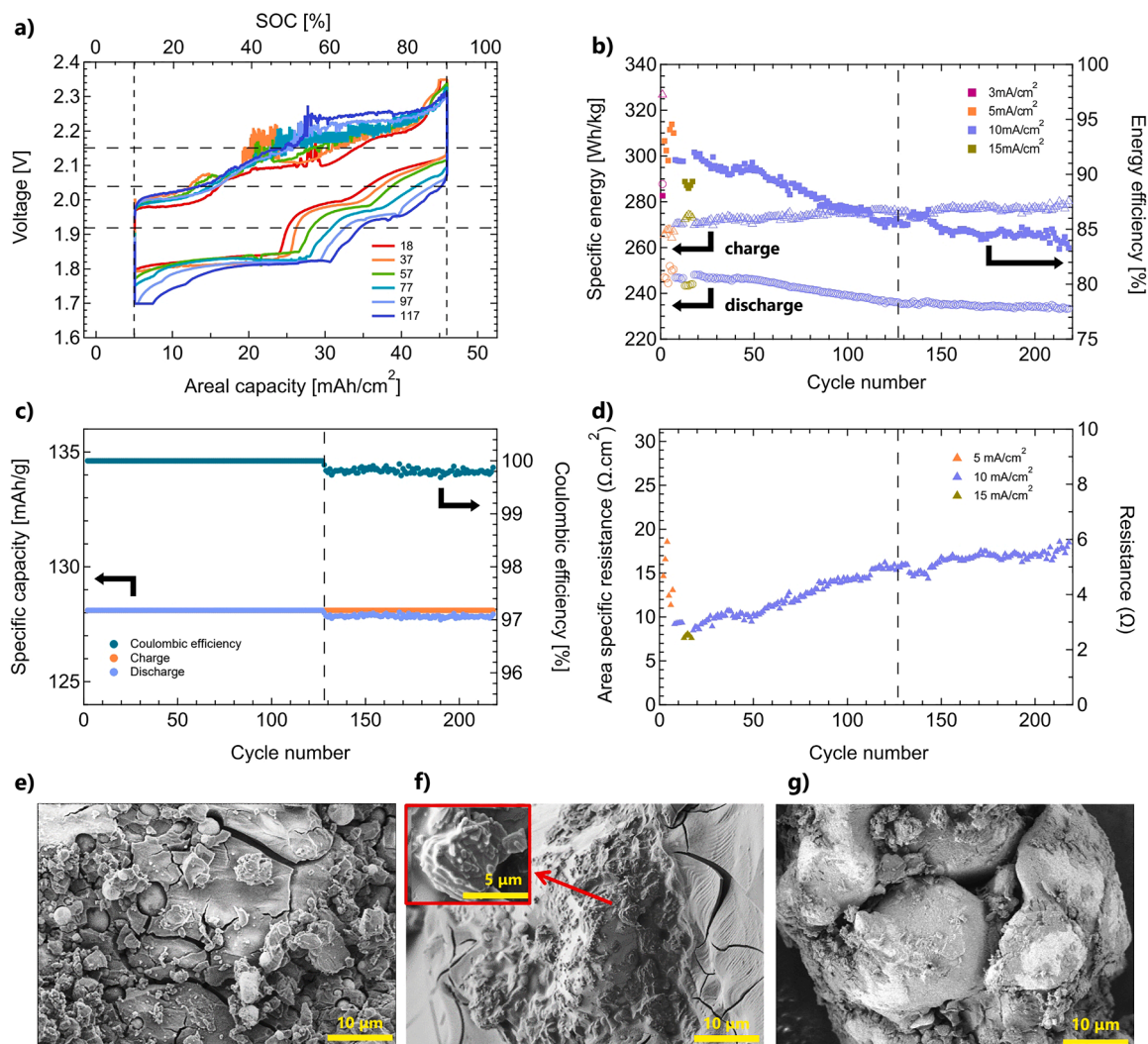

Fig. 6. Extended cycling of Na-ZnCl$_2$ cell with cathode pellet (30% active Zn) at 10 mA/cm^2, 300 °C. a) Galvanostatic voltage-capacity profiles of cycles 1, 20, 40, 60, 80 and 100. b) Dis-/charge energy and energy efficiency per cycle. c) Dis-/charge capacity and coulombic efficiency per cycle. d) Average cell resistance per cycle. e) Pristine microstructure of Zn/NaCl cathode at 0% SOC, after infiltration with NaAlCl$_4$. f) Postmortem microstructure of the same cathode at 100% SOC, showing ZnCl$_2$ grains with sheet-like morphology (inset). g) Postmortem microstructure of zinc particles, after removal of NaAlCl$_4$.

sample (0.14 S/cm vs. 0.18 S/cm at 300 °C, see **Figure S9**). This conductivity decrease accounts for an increase in cell resistance by $<0.2\ \Omega$ cm^2 at a current density of 10 mA/cm^2, and is therefore not a major cause for the resistance increase by $\sim10\ \Omega$ cm^2. As shown in Fig. 6e-g, the degradation in cycling performance is accompanied by significant changes of the cathode microstructure. As discussed in Fig. 2, the pristine cathode contains NaCl powder and fine spherical zinc particles ≤ 5 μm (0% SOC). Fig. 6e displays a cross-section of the cathode pellet after vacuum infiltration with molten NaAlCl$_4$, which shows that the particle microstructure is maintained after this process. While mostly covered by the secondary electrolyte, we can distinguish the spherical morphology of the fine zinc particles. After cycling, however, the cathode microstructure coarsens significantly. Fig. 6f shows the cathode postmortem at 100% SOC, which now also contains ZnCl$_2$ grains with a sheet-like morphology (see inset). The ZnCl$_2$ is present in its monoclinic (γ) crystalline form, as identified through XRD (**Figure S10**). Despite a moderate active metal content of 30%, fine spherical zinc particles are no longer visible. Removal of NaAlCl$_4$ by washing in isopropanol reveals that all remaining zinc has agglomerated into much larger ($>> 10$ μm), partially interconnected particles with variable morphology. This indicates that microstructural coarsening, driven by agglomeration of zinc particles, was a major cause of degradation in this particular Na-ZnCl$_2$ cell.

Conclusions

Firstly, our study on Zn/NaCl and Ni/NaCl model cathodes showed that the filamentary morphology of Ni255 facilitates electronic percolation, which was maintained even at 7 vol% of Ni powder. With spherical Zn powder, electronic percolation was disturbed when the volume fraction of Zn decreased to 21 vol% (40% active Zn) and below. Furthermore, the spherical morphology of the zinc powder resulted in a higher relative density (+10%), which impaired infiltration of the secondary electrolyte. Based on these results, we tailored the composition of cathode granules and cathode pellets with 30% active metal content to maintained electronic percolation down to a Zn volume fraction of 20 vol% at an areal capacity of $\sim$50 mAh/cm^2.

Secondly, we related the succession of phases in the cathode during cycling of Na-ZnCl$_2$ cells to the corresponding ternary NiCl$_2$-NaCl-AlCl$_3$ phase diagram at 300 °C. However, during continuous cycling at 5–15 mA/cm^2, the electrochemical behavior of the present system is more similar to the binary ZnCl$_2$-NaCl phase diagram. This indicates that, in the conditions adopted for this study, the secondary NaAlCl$_4$ electrolyte does not mix with other chloride species, as predicted for thermodynamic equilibrium. This sets a basis to study the relevant reaction and aging mechanisms in Na-ZnCl$_2$ cells in more detail in further studies. We further demonstrated the influence of cathode microstructure on the electrochemical cycling performance of cells with Zn/NaCl cathode pellet or cathode granules. In early cycles, cathode granules provided lower overpotentials, with energy efficiencies around 94% at a current density of 10 mA/cm^2 (vs. 91% for cathode pellets). Nevertheless, cells assembled with cathode granules systematically showed an early failure, while long term cycling was achieved with the new pellet formulation. For the latter, 217 cycles were conducted at an operating temperature of 300 °C ($\sim$3 months), and a cumulative capacity of 8.9 Ah/cm^2 was transferred at energy efficiencies >83% at C/5.

Thirdly, postmortem analyses of the ceramic Na-β''-alumina electrolyte indicated only minor degradation in terms of ion conductivity. Instead, significant microstructural coarsening and agglomeration of zinc particles at the cathode were revealed as a major cause of degradation of this cell. Future studies should focus on stabilizing the cathode microstructure. Similar to state-of-the-art Na-NiCl$_2$ batteries, this could be achieved by the use of suitable additives [22,23,44-46]. Furthermore, integration of structural elements[23] or limitations of the SOC range to selected phase regions [17] are promising options.

Supplemental information

Supplemental material associated with this article can be found in the online version.

CRediT authorship contribution statement

Louis Sieuw: Conceptualization, Formal analysis, Investigation, Methodology, Visualization, Writing – original draft, Writing – review & editing. **Tu Lan:** Writing – original draft. **Enea Svaluto-Ferro:** Investigation, Validation. **Fabrizio Vagliani:** Investigation. **Sumit Kumar:** Investigation. **Wenjin Ding:** Investigation. **Alberto Turconi:** Investigation, Validation. **Diego Basso:** . **Andrea Pozzi:** . **Corsin Battaglia:** Project administration, Supervision, Writing – review & editing. **Meike V.F. Heinz:** Conceptualization, Formal analysis, Funding acquisition, Methodology, Project administration, Supervision, Visualization, Writing – original draft, Writing – review & editing.

Declaration of Competing Interest

The authors declare that they have no known competing financial interests or personal relationships that could have appeared to influence the work reported in this paper.

Data availability

Datasets related to this article are available at doi.org/10.5281/zenodo.8249437.

Acknowledgments

Supplementary materials

Supplementary material associated with this article can be found, in the online version, at doi:10.1016/j.ensm.2023.103077.

References

[1] R. Benato, et al., Sodium nickel chloride battery technology for large-scale stationary storage in the high voltage network, J. Power Sources 293 (2015) 127–136, https://doi.org/10.1016/j.jpowsour.2015.05.037.

[2] Benato, R. et al. in *AEIT 2016 - International Annual Conference: Sustainable Development in the Mediterranean Area, Energy and ICT Networks of the Future.* 1-5.

[3] K. Frutschy, T. Chatwin, R. Bull, Cell overcharge testing inside sodium metal halide battery, J. Power Sources 291 (2015) 117–125, https://doi.org/10.1016/j.jpowsour.2015.05.001.

[4] J. Matheys, et al., Influence of functional unit on the life cycle assessment of traction batteries, Int. J. Life Cycle Assess. 12 (2007) 191, https://doi.org/10.1065/lca2007.04.322. –191.

[5] S. Longo, V. Antonucci, M. Cellura, M. Ferraro, Life cycle assessment of storage systems: the case study of a sodium/nickel chloride battery, J Clean Prod 85 (2014) 337–346, https://doi.org/10.1016/j.jclepro.2013.10.004.

[6] A. Accardo, G. Dotelli, M.L. Musa, E Spessa, Appl. Sci. 11 (2021).

[7] M.V.F. Heinz, G. Graeber, D. Landmann, C. Battaglia, Pressure management and cell design in solid-electrolyte batteries, at the example of a sodium-nickel chloride battery, J. Power Sources 465 (2020), 228268, https://doi.org/10.1016/j.jpowsour.2020.228268. –228268.

[8] T. Lan, et al., Planar sodium-nickel chloride batteries with high areal capacity for sustainable energy storage, Adv. Funct. Mater. (2023), https://doi.org/10.1002/adfm.202302040.

[9] X. Lu, et al., The effects of temperature on the electrochemical performance of sodium-nickel chloride batteries, J. Power Sources 215 (2012) 288–295, https://doi.org/10.1016/j.jpowsour.2012.05.020.

[10] G. Li, et al., Advanced intermediate temperature sodium-nickel chloride batteries with ultra-high energy density, Nat. Commun. 7 (2016) 10683, https://doi.org/10.1038/ncomms10683. –10683.

[11] H.J. Chang, et al., Development of intermediate temperature sodium nickel chloride rechargeable batteries using conventional polymer sealing technologies,

J. Power Sources 348 (2017) 150–157, https://doi.org/10.1016/j.jpowsour.2017.02.059.

[12] B.M. Ahn, et al., Effect of cathode microstructure on electrochemical properties of sodium nickel-iron chloride batteries, Materials (Basel) 14 (2021), https://doi.org/10.3390/ma14195605.

[13] H.J. Chang, et al., "Ni-less" cathodes for high energy density, intermediate temperature Na–NiCl2 batteries, Adv. Mater. Interfaces 5 (2018), 1701592, https://doi.org/10.1002/admi.201701592. –1701592.

[14] X. Zhan, et al., A low-cost durable Na-FeCl2 battery with ultrahigh rate capability, Adv. Energy Mater. 10 (2020), https://doi.org/10.1002/aenm.201903472.

[15] G. Graeber, et al., Rational cathode design for high-power sodium-metal chloride batteries, Adv. Funct. Mater. 31 (2021), 2106367, https://doi.org/10.1002/adfm.202106367. –2106367.

[16] M.V.F. Heinz, et al., Cell design strategies for sodium-zinc chloride (Na-ZnCl2) batteries, and first demonstration of tubular cells with 38 Ah capacity, Electrochim. Acta 464 (2023), 142881, https://doi.org/10.1016/j.electacta.2023.142881. –142881.

[17] X. Lu, et al., A novel low-cost sodium-zinc chloride battery, Energy Environ. Sci. 6 (2013) 1837–1843, https://doi.org/10.1039/c3ee24244g.

[18] X. Lu, et al., An intermediate-temperature high-performance Na-ZnCl2 battery, ACS Omega 3 (2018) 15702–15708, https://doi.org/10.1021/acsomega.8b02112.

[19] Y. Lee, et al., Electrochemically activated Na–ZnCl2 battery using a carbon matrix in the cathode compartment, J. Power Sources 440 (2019), 227110, https://doi.org/10.1016/j.jpowsour.2019.227110. –227110.

[20] P. Parthasarathy, N. Weber, A.V. Virkar, High temperature sodium - zinc chloride batteries with sodium beta - alumina solid electrolyte, ECS Trans. 6 (2007) 67–76, https://doi.org/10.1149/1.2811944.

[21] O.E. Godinez-Brizuela, D. Niblett, K.E. Einarsrud, Microstructural analysis of effective electrode conductivity in molten salt, Na-ZnCl2 batteries, J. Electrochem. Soc. 169 (2022) 90510, https://doi.org/10.1149/1945-7111/ac8edd. –90510.

[22] R.C. Galloway, S. Haslam, The ZEBRA electric vehicle battery: power and energy improvements, J. Power Sources 80 (1999) 164–170, https://doi.org/10.1016/S0378-7753(98)00259-6.

[23] J.L. Sudworth, The sodium/nickel chloride (ZEBRA) battery, J. Power Sources 100 (2001) 149–163, https://doi.org/10.1016/S0378-7753(01)00891-6.

[24] Y. Li, et al., Ni-less cathode with 3D free-standing conductive network for planar Na-NiCl2 batteries, Chem. Eng. J. 387 (2020), 124059, https://doi.org/10.1016/j.cej.2020.124059. –124059.

[25] S.W. Orchard, G. Mamantov, An electrochemical and spectroelectrochemical study of the behavior of cobalt electrodes in molten aluminum chloride: sodium chloride mixtures, J. Electrochem. Soc. 136 (1989) 3565–3570, https://doi.org/10.1149/1.2096510.

[26] B.V. Ratnakumar, S. Di Stefano, G. Halpert, Electrochemistry of metal chloride cathodes in sodium batteries, J. Electrochem. Soc. 137 (1990) 2991–2997, https://doi.org/10.1149/1.2086147.

[27] B.V. Ratnakumar, A.I. Attia, G. Halpert, Sodiummetal chloride battery research at the Jet Propulsion Laboratory (JPL), J. Power Sources 36 (1991) 385–394, https://doi.org/10.1016/0378-7753(91)87014-3.

[28] B.V. Ratnakumar, A.I. Attia, G. Halpert, Alternate cathodes for sodium—metal chloride batteries, J. Electrochem. Soc. 138 (1991) 883, https://doi.org/10.1149/1.2085704. –883.

[29] J. Coetzer, G.D. Wald, S.W. Orchard, Mechanism of the cathode reaction in sodium-ferrous chloride secondary cells, J. Appl. Electrochem. 23 (1993) 790–800, https://doi.org/10.1007/BF00249951.

[30] R.C. Galloway, A sodium/beta-alumina/nickel chloride secondary cell, J. Electrochem. Soc. 134 (1987) 256–257, https://doi.org/10.1149/1.2100421.

[31] C.H. Dustmann, Advances in ZEBRA batteries, J. Power Sources 127 (2004) 85–92, https://doi.org/10.1016/j.jpowsour.2003.09.039.

[32] G. Li, et al., An Advanced Na-FeCl2 ZEBRA Battery for Stationary Energy Storage Application, Adv. Energy Mater. 5 (2015), 1500357, https://doi.org/10.1002/aenm.201500357. –1500357.

[33] X. Zhan, M.M. Li, J.M. Weller, V.L. Sprenkle, G. Li, Recent progress in cathode materials for sodium-metal halide batteries, Materials (Basel) 14 (2021), https://doi.org/10.3390/ma14123260.

[34] X. Gao, et al., An in-situ alloyed Ni-Fe Co-reaction electrode for high-stability and high-rate Na-metal halide batteries, Mater. Today Energy 23 (2022), 100894, https://doi.org/10.1016/j.mtener.2021.100894. –100894.

[35] B.-M. Ahn, et al., Batteries 8 (2022).

[36] D. Landmann, E. Svaluto-Ferro, M.V.F. Heinz, P. Schmutz, C. Battaglia, Elucidating the rate-limiting processes in high-temperature sodium-metal chloride batteries, Adv. Sci. (Weinh) 9 (2022), e2201019, https://doi.org/10.1002/advs.202201019.

[37] G. Róg, A. Kozlowska-Róg, Divalent ion-β''-alumma electrolytes for the study of thermodynamic properties of oxide systems, Z. Phys. Chem. 207 (1998) 83–92, https://doi.org/10.1524/zpch.1998.207.Part_1_2.083.

[38] Y. Yung-Fang Yu, J.T. Kummer, Ion exchange properties of and rates of ionic diffusion in beta-alumina, J. Inorg. Nucl. Chem. 29 (1967) 2453–2475, https://doi.org/10.1016/0022-1902(67)80301-4.

[39] D. Landmann, G. Graeber, M.V.F. Heinz, S. Haussener, C. Battaglia, Sodium plating and stripping from Na-β''-alumina ceramics beyond 1000mA/cm2, Mater. Today Energy 18 (2020), 100515, https://doi.org/10.1016/j.mtener.2020.100515. –100515.

[40] M.C. Bay, et al., Impact of liquid phase formation on microstructure and conductivity of Li-stabilized Na-β''-alumina ceramics, ACS Appl. Energy Mater. 2 (2019) 687–693, https://doi.org/10.1021/acsaem.8b01715.

[41] M.V.F. Heinz, M.C. Bay, U.F. Vogt, C. Battaglia, Grain size effects on activation energy and conductivity: Na-β''-alumina ceramics and ion conductors with highly resistive grain boundary phases, Acta Mater. 213 (2021), 116940, https://doi.org/10.1016/j.actamat.2021.116940. –116940.

[42] C.H. Kuo, P.K. Gupta, Rigidity and conductivity percolation thresholds in particulate composites, Acta Metall. Mater. 43 (1995) 397–403, https://doi.org/10.1016/0956-7151(95)90296-1.

[43] S. Kumar, et al., AlCl3-NaCl-ZnCl2 secondary electrolyte in next-generation ZEBRA (Na-ZnCl2) battery, Batteries 9 (2023), https://doi.org/10.3390/batteries9080401.

[44] R.J. Bones, D.A. Teagle, S.D. Brooker, F.L. Cullen, Development of a Ni, NiCl2 positive electrode for a liquid sodium (ZEBRA) battery cell, J. Electrochem. Soc. 136 (1989) 1274–1277, https://doi.org/10.1149/1.2096905.

[45] B.V. Ratnakumar, S. Surampudi, G. Halpert, Effects of sulfur additive on the performance of Na/NiCl2 cells, J. Power Sources 48 (1994) 349–360, https://doi.org/10.1016/0378-7753(94)80031-6.

[46] J. Prakash, L. Redey, D.R. Vissers, J. DeGruson, Effect of sodium iodide additive on the electrochemical performance of sodium/nickel chloride cells, J. Appl. Electrochem. 30 (2000) 1229–1233, https://doi.org/10.1023/A:1026539607417.